ION CYCLOTRON RANGE OF FREQUENCY POWER:
Progress in Operation and Understanding for Experiments with Metallic Walls

J.-M. NOTERDAEME[1,2,*], V. BOBKOV[1], YE. O. KAZAKOV[3], A. KOSTIC[2,1], R. OCHOUKOV[1], I. SHESTERIKOV[1], W. TIERENS[1], M. USOLTCEVA[2,1], W. ZHANG[1,4], D. AGUIAM[5], R. BILATO[1], L. COLAS[6], K. CROMBÉ[2,3], H. FAUGEL[1], J. FAUSTIN[7], H. FUENFGELDER[1], S. HEURAUX[8], A. KAPPATOU[1], R. MAGGIORA[9], M. MANTSINEN[10,11], A. MESSIAEN[3], D. MILANESIO[9], J. ONGENA[3], R. RAGONA[3,2], A. SILVA[5], G. SUÁREZ LÓPEZ[1,12], D. VAN EESTER[3], M. WEILAND[1], the ASDEX UPGRADE[1] and EUROFUSION MST1** TEAMS

[1] Max-Planck-Institut für Plasmaphysik, D-85748 Garching, Germany
[2] Ghent University, Applied Physics Department, B-9000 Gent, Belgium
[3] LPP-ERM/KMS, B-1000 Brussels, Belgium
[4] ASIPP, Institute of Plasma Physics, Chinese Academy of Sciences, Hefei, China
[5] Instituto de Plasmas e Fusão Nuclear, IST, 1049-001 Lisboa, Portugal
[6] CEA, IRFM, F-13108 Saint-Paul-Lez-Durance, France
[7] Max-Planck-Institut für Plasmaphysik, D-17491 Greifswald, Germany
[8] IJL UMR 7198 CNRS-Université de Lorraine, BP70239, F-54506 Vandoeuvre, France
[9] Politecnico de Torino, Torino, Italy
[10] Barcelona Supercomputing Center (BSC), 08034 Barcelona, Spain
[11] ICREA, Pg. Lluis Companys 23, 08010 Barcelona, Spain
[12] Ludwig-Maximilian-University of Munich, D-80539 Munich, Germany
[*] e-mail: noterdaeme@ipp.mpg.de
[**] see the author list H. Meyer et al, 2017 Nucl. Fusion 57 102014

Abstract

Significant progress in applying ICRF power to ASDEX Upgrade (AUG) through improved power coupling and reduced impurity production has been associated with progress in understanding and modelling. First, the coupling of the fast wave was improved using outer mid-plane gas injection. The local edge density increase in front of the antenna shifts the fast wave cut-off position closer to the antenna by ~2cm, a result confirmed with new density measurements in front of the antenna. The ICRF coupling increases by 120% (only 25% for top gas puffing). The increased density and resulting improved coupling. was also numerically modelled. Second, the new 3-strap antennas in AUG demonstrated clearly that a proper antenna design can successfully mitigate ICRF-specific tungsten (W) sputtering. The reduction of the W sputtering was achieved by minimizing the RF currents on the antenna surfaces exposed to the scrape-off-layer (SOL) plasma. The local RF currents, rectified DC currents and the W sputtering yield at the antenna side limiters experience a clear minimum close to a phasing between the central and the outer straps of 180° and a power balance ratio P_{cen}/P_{out} of ~ 2. At this optimum, the local source of sputtered W at the limiters is reduced by a factor between 1.5 and 6, depending on the location. The experiments and modelling confirm the hypothesis of sheath rectification as the source of the sputtered W. Furthermore, the new 3-ion ICRF heating scenario, which can produce very energetic particles, has been successfully reproduced in AUG. The progress in operation, in understanding and modelling is strongly supported by improved ICRF diagnostic coverage including density measurements directly in front of the antenna by reflectometry, advanced RF coupling characterization, measurements of antenna limiter currents, B-dot probes, Ion Cyclotron Emission (ICE) measurements and by dedicated tests on the experimental device IShTAR (Ion cyclotron Sheath Test ARrangement).

1. INTRODUCTION

ASDEX Upgrade (AUG) is a medium size divertor tokamak (R = 1.65m, a = 0.5m, b=0.8m, B_t < 3.1T, I_p < 1.2 MA) with three heating methods: two neutral beam injectors deliver a total of up to 20 MW in deuterium beams at energies of 60keV and 93 keV, electron cyclotron power is available with up to 8MW at 140 GHz or 6.4 MW at 105 GHz. Power in the ion cyclotron range of frequencies is delivered by four antennas, powered by 4 generators in an ELM-resilient configuration with a total power of originally 8 MW and a frequency range of 30 to 60 MHz (and with reduced power capability at higher frequencies). Up to 6 MW have been coupled at 30 MHz. Starting 2018, an additional generator will be available to increase the installed power capability to 9.5 MW.

Over the years, AUG has evolved from a carbon (C) machine to machine where all first wall components are made of tungsten (W) or are W coated. Major results obtained consist of the achievement of H-mode [1], the development of an ELM-resilient coupling system [2], the use of ^{3}He as minority [3], the test of an antenna without Faraday screen [4], application of the central ICRF to avoid impurity accumulation in various scenarios including

the ITER baseline [5], generation of MHD modes by the ICRF-accelerated ions [6], application of the Ion Cyclotron Wall Cleaning (ICWC) techniques [7]. Since the change to an all W machine, the need to understand the plasma-antenna interactions and to eliminate the increased impurity production due to the ICRF power has grown in importance. Whereas the antennas were originally 4 identical 2-strap antennas [8], they now consist of a pair of 2-strap antennas, with boron (B) coated limiters and a pair of 3-strap antennas with W coated limiters.

In addition to the experimental programme, understanding was improved by using theoretical modelling, assisted by data from sepcific diagnostics [9] and a supporting programme on a test stand (IShTAR) [10].

We report here on the recent advances that allowed experimentally to suppress significantly (and often completely) the ICRF-specific impurity production; these advances were accompanied by code developments. The density in front of the antenna plays a large role in the power coupling. With the help of a new edge reflectometer diagnostic, we have shown experimentally and confirmed theoretically that the edge density profile in front of the antenna can be modified to increase the antenna coupling. We have also modelled and confirmed experimentally that, in case the 3-strap antennas do not operate in their optimized configuration, convective cells can develop in front of the antennas. A new 3-ion ICRF scenario, theoretically predicted [11, 12], and experimentally tested on Alcator C-mod and JET [13], has further been investigated on AUG. In section 5, we give an overview of the recent developments of dedicated diagnostics, and in the last section, the accompanying programme on IShTAR is presented.

2. OPTIMIZATION OF THE ANTENNA GEOMETRY

After the AUG ICRF antenna limiters were replaced by the W-coated ones, the ICRF power from the original 2-strap antennas led to a strong increase of the plasma W content and high radiated power, negatively affecting the performance [14]. Spectroscopic measurements of the W erosion at the antenna limiters [15] confirmed that the W influx correlated strongly with the ICRF power. The ways to improve the antenna design and experimental conditions were at first assessed [16] by using RF near-field calculation. Further development of the theoretical description of the mechanisms driving the RF sheaths deemed responsible for the W sputtering, has been improved significantly in the recent years [17], partially due to more experimental data becoming available.

2.1. Experimental results

First experiments tested a 2-strap antenna in which shields covered the antenna corners where magnetic field lines pass only in front of one strap. These locations were initially considered as candidates to explain the appearance of the RF sheaths leading to the W sputtering. However, more advanced calculations, confirmed by experiments indicated that this modification does not lead to significant change of the W sputtering pattern [16]. This demonstrated that the RF fields at the Faraday Screen have a limited contribution to the limiter W erosion, and rather that the fields at the antenna frame (including the limiters) need to be reduced to reduce W sputtering.

For the second experimental step, one original 2-strap antenna was modified by introducing narrower straps and broader antenna limiters, in order to reduce the RF image current density at the limiters that drives the local RF electric fields including the parallel component $E_{\|}$. The latter had been assumed to be the most probable candidate to explain the mechanism driving the RF sheaths and thus the elevated plasma potentials which lead to ion acceleration and W sputtering. Indeed, the experiments showed a reduction of up to 40% of the sputtering yield measured at the limiters of the modified antenna, consistent with the core W content which was similarly smaller when the modified antenna was operated [18].

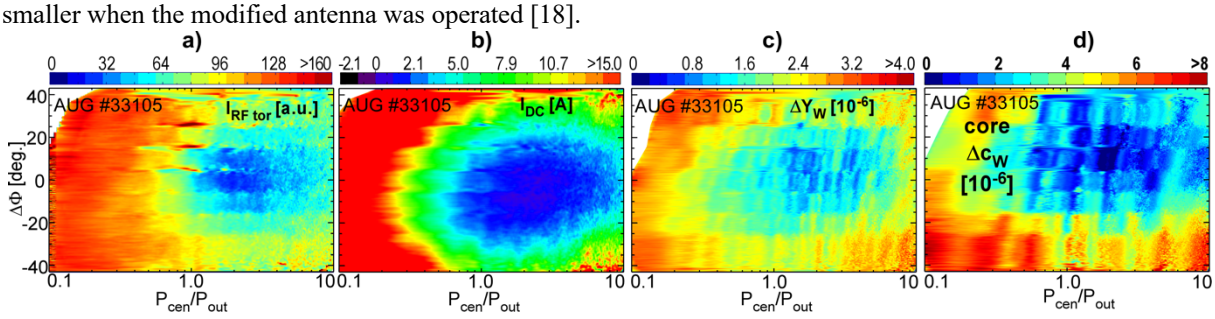

FIG. 1. RF feeding diagrams using the strap power balance P_{cen}/P_{out} and phase deviation from dipole $\Delta\Phi$ as variables in a discharge with P_{ICRF}=1MW; local measurements at a single antenna limiter tile of (a) the toroidal RF current, (b) the DC current circulation and (c) of the increment of the W sputtering yield; (d) increment of the W content in plasma at T_e≈1.5 keV.

The third and most significant step was to build and install new 3-strap antennas [19] which were designed to minimize the RF image current in the antenna frame and the electric fields (including $E_{||}$) at the lateral antenna limiters. The accompanying upgrade of the circuit feeding the antenna allowed the experimental characterization of the formation of the RF sheaths and W sputtering (Fig. 1) with the power balance parameter P_{cen}/P_{out} (ratio of the power launched by the central strap to that by both outer straps) and phase deviation from dipole $\Delta\Phi$ as variables. Figure 1 presents the RF current, rectified DC current and the sputtering yield measured at one of the limiter tiles, as well as the ICRF specific increment of the W concentration in the plasma (see [20] for details). Depending on antenna location, the W sources decrease by a factor of 1.5 to 6 for the optimized configuration [21]. Compared to the W-coated 2-strap antennas, the 3-strap antennas [22] showed a drastic decrease of the ICRF-specific W content, provided these were operated close to the optimal configuration (dipole phasing and $P_{cen}/P_{out} \approx 2$). The impurity performance was at the same level or better than the 2-strap antenna with B-coated limiters.

2.2. Development of codes

The observed minima of the RF current and $E_{||}$ at the limiters can be well reproduced by near-field calculations using a simplified description with a vacuum layer between the antenna and the plasma [21, 22]. More sophisticated analyses with RAPLICASOL and SSWICH codes [23], which take into account more realistic wave propagation in the scrape-off-layer, confirmed that for the 3-strap antenna minima are observed both for $E_{||}$ and for the rectified potential at the limiters for the proper power ratio and phasing. The RAPLICASOL code [24, 25], used to model ICRF wave propagation and power coupling near the antenna, is now able to handle curved geometries, complete with corresponding curved Perfectly Matched Layers [26], and to import not only an arbitrary 3D density profile from experiments and EMC3-Eirene simulations, but also an arbitrary 3D vector field for the confining magnetic field. Great progress has also been made in the validation of RAPLICASOL against other ICRF codes such as TOPICA [24]. We found that RAPLICASOL and TOPICA predict similar reflection coefficients (to within ~2%). Other quantities of experimental interest which depend on the reflection coefficients, such as the coupled power, coupling resistance, and optimal matching settings, were also found to be in good agreement between both codes. TOPICA itself was in agreement with extensive experimental comparisons [27].

3. DENSITY PROFILE IN FRONT OF THE ANTENNA

The density profile directly in front of the antenna plays a significant role in the antenna coupling. New diagnostic capabilities (reflectometry directly in front of the antenna) and new modelling capabilities allowed significant advances in the calculation of the modifications of this density profile, which then could be confirmed by the experimental data.

3.1. Increase in coupling through gas puffing

The coupling of ICRF power to the plasma depends sensitively on the plasma density in front of the antennas since the launched fast wave is evanescent below the cut-off density (usually of the order of 10^{18} m^{-3} for typical frequencies and antenna spectra in present day tokamak). The local density in front of the antenna and thus the ICRF coupling can be increased with local gas puffing/fuelling. In recent AUG experiments [28], midplane gas puffing close to the ICRF antenna was found to increase the ICRF power coupling most significantly (~120%) while top gas puffing increases it to a much smaller level (~25%) in typical H-mode plasmas with a moderate gas rate of 1.2 x 10^{22} el/s. In parallel with experiments, the 3D edge plasma fluid and neutral particle transport code EMC3-EIRENE [29] is used to calculate the SOL density profiles for different gas puffing scenarios; the calculated profiles are then used in the antenna codes such as FELICE [30] and RAPLICASOL [25] to calculate the coupling resistances. The simulation results are in good agreement with the experimental results [31, 32]. They indicate that midplane gas puffing increases the SOL density very significantly at locations locally close to the gas valve, and this increase decays exponentially as a function of geometrical distance between the gas valve and antenna. Top gas puffing increases the SOL density almost toroidally homogeneously but at a smaller level, and this increase is independent of the toroidal positions of the gas valves. The effects of local gas puffing on local plasma density are attributed to the localized high neutral density (gas cloud), magnetic field line connections to the gas cloud and the local decrease of the temperature [32-34].

Further EMC3-EIRENE simulations have been carried out for ITER [35] and DEMO [36]. The results suggest that in order to maximize ICRF coupling in these future machines, gas should be injected as close as possible to the ICRF antenna locations while keeping the gas cloud covering the antenna as much as possible. In ITER,

midplane gas puffing close to the antenna could increase the coupling resistance by ~150%-200% for typical H-mode with standard density profiles.

3.2. Convective cells

While the antenna is designed to launch the fast wave, the slow wave is generated parasitically. The nonlinear interaction between the slow wave and sheath results in enhanced inhomogeneous sheath potentials and formation of E×B convective cells in the SOL, leading to density modifications in the SOL. To understand the ICRF induced SOL modifications, two methods have been developed: 1) EMC3-EIRENE simulations based on the experimental data (using the potential measured with a RFA probe) [37], and 2) self-consistent simulations by running the EMC3-EIRENE, RAPLICASOL and SSWICH [38] codes in an iterative way [39]. The calculated density convection can then be compared with the density measurements, obtained from the reflectometers embedded in the antenna [40]. Good qualitative agreement between simulation and measured density convection has been obtained. Our results indicate that the largest sheath potential, convective cells and thus density convection are located on the top and bottom of the antenna. Density depletions are seen inside the convective cells while density accumulations are developed where the convective cells interact with the wall. The 3-strap antenna with optimized antenna feeding configuration (dipole phasing, power ratio between central and outer straps=2:1) leads to the lowest the sheath potential and density convection among the studied cases.

The RF convective cells can also influence the turbulence transport and further modify the SOL density. Recent progress has been achieved on understanding the interaction between the turbulence and RF convective cells [41]. It is shown that RF convective cells can distort and even break up the big blobs into small ones in the SOL. Self-consistent simulations by running the BOUT ++ [42], RAPLICASOL and SSWICH codes are expected to further address the underlying physics.

4. NEW 3-ION ICRF HEATING SCENARIO

The novel three-ion species ICRH scheme has been recently demonstrated as an efficient technique for heating various mixed ions plasmas [13], also holding promises for future ITER operations [43]. Following JET and Alcator C-Mod experiments, minority heating of ^{3}He ions in H-D plasmas has been successfully demonstrated on AUG.

The experiments were carried out in H-D mixed plasmas with H/(H+D) ≈ 0.7- 0.8 at a magnetic field of 3T and 2.8T, and a plasma current of 800kA. Up to 2.6MW of ICRF power was coupled into the plasma at f = 30MHz. This choice of RF frequency and magnetic field places the cyclotron resonance of the ^{3}He minority ions in the plasma core for discharges at 3T and at the high-magnetic field side (HFS) at $\rho_{pol} \approx 0.3$ for discharges at 2.8T. Hydrogen neutral beams (up to 8MW) were applied for plasma pre-heating and charge exchange recombination spectroscopy (CXRS) measurements. In the absence of a real-time control scheme for the ^{3}He concentration, a series of short (50ms) ^{3}He puffs from a gas valve at the mid-plane were applied. The ^{3}He puff rate ([2-18]×10^{20} el/s) and the inter-puff interval were varied from shot to shot in order to assess the sensitivity of the heating scenario ^{3}He concentration in the core and to optimize the scenario performance on AUG. According to numerical computations, conditions of efficient double-pass wave absorption for this scenario can be achieved on AUG for ^{3}He concentrations in the range $X[^3He] = n(^3He)/n_e \approx 0.2\text{-}1.5\%$. At higher ^{3}He concentrations, a mode conversion heating regime is reached, characterized by a fairly low double-pass absorption efficiency (~10-30%).

Controlling the ^{3}He concentration is a key factor in determining the performance of this ICRF scenario on AUG. Operation at relatively high ^{3}He concentrations of ~3-5% resulted in low heating performance and increased W content, in line with modelling results predicting low double-pass wave absorption under these conditions. Figure 2(a) shows an evolution of plasma parameters for AUG discharge #34697 with on-axis ^{3}He resonance. High ^{3}He puff rates of 18×10^{20} el/s and 17×10^{20} el/s were applied for the first (t = 1.35-1.40s) and second (t = 2.35-2.40s) puffs, respectively.

The second panel of Fig. 2(a) shows the temporal evolution of the total helium concentration (^{3}He and ^{4}He) in the plasma, as measured by the CXRS system. Most of the measured helium content comes from ^{3}He, and the ^{3}He concentration increases rapidly after each ^{3}He puff and then decays.

Strongly radially peaked ion temperature profiles with $T_i(0)$ up to 4.3 keV were observed during the ICRF+NBI phase of the discharge after the first ^{3}He puff, when the He concentration decayed from ~4% to ~1.3-2%. For comparison, the core ion temperature during the NBI-only phase reached $T_i(0) \approx 1.9$keV. Unfortunately, $T_e(0)$ data is not available for AUG discharges at 2.8-3T, making the analysis of the peakedness of the T_e profile

and comparison of T_e and T_i profiles difficult to assess. We note that for #34697 with relatively high ^{3}He concentration, T_e at $\rho_{pol} \approx 0.2$ closely matched the corresponding T_i value.

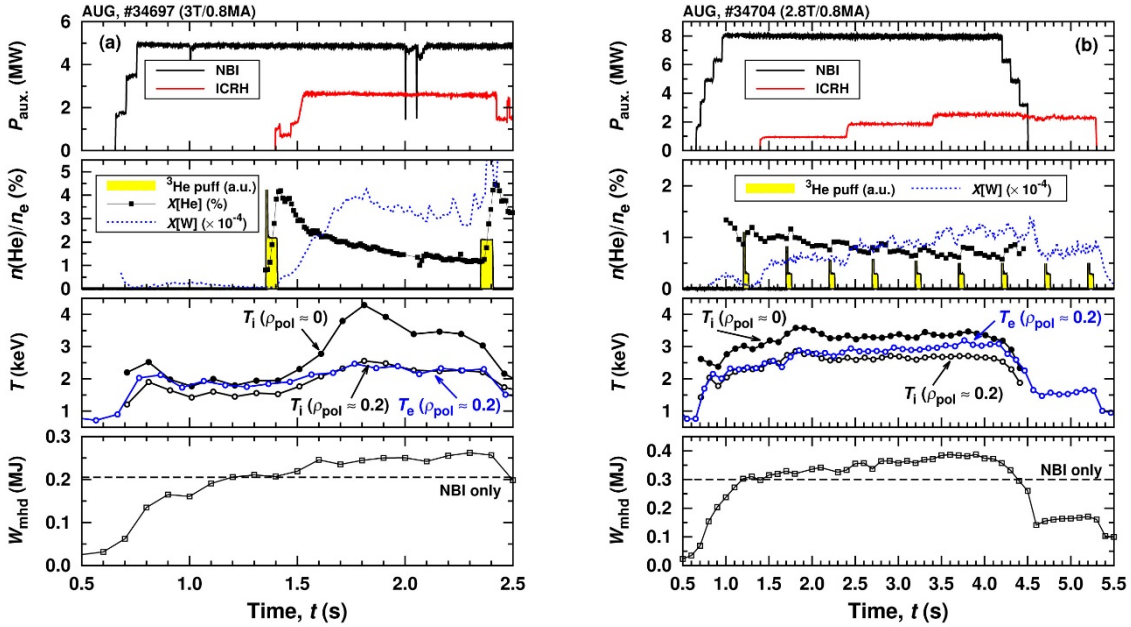

FIG 2: Overview of plasma parameters for AUG discharge #34697 with a central ^{3}He ICRF resonance (3T, f = 30MHz) and discharge #34704 with a HFS off-axis ^{3}He resonance (2.8T, f = 30MHz). T_i and T_e were measured with the CXRS and Thomson Scattering systems, respectively. The displayed data is averaged over the time interval of 100 ms.

Interestingly, similar to the T_i profile, the plasma toroidal rotation velocity also had a peaked profile, increasing from 100 km/s during the NBI-only phase to 230 km/s during the ICRF+NBI phase. These observations are quite similar to the ones reported for ^{3}He minority heating scenario in deuterium plasmas on AUG [44]. Whether this effect is due to ICRF fast-ion and heating physics, or is caused by the changes in the transport properties of the plasma (e.g. due to increased central radiation) needs further analysis.

With on-axis heated ICRF discharges, an efficient generation of energetic ^{3}He ions was observed, confirmed by the excitation of Alfvén modes ($f_{AE} \approx$ 160-190 kHz), the appearance of fishbones and measurements with the fast-ion loss detector (FILD). Backward-orbit tracing of ions measured by FILD infers an acceleration of ^{3}He ions to the energies of at least ~1.7 MeV for the ICRF resonance at the center. In a few discharges, no ^{3}He was injected into the plasma and the heating scenario relied on the residual ^{3}He left from the previous discharges. Although Alfvén modes were observed in such plasmas, heating AUG plasmas with the three-ion scenario at extremely low ^{3}He concentrations did not show such clear signs as on JET, for which ^{3}He concentrations as low as ~0.2% were successfully used for plasma heating [11].

In contrast to JET, medium-size AUG plasmas cannot confine multi-MeV energetic ions, which are generated with this ICRF scenario at extremely low^{3}He concentrations. In order to improve the confinement of the RF-heated ^{3}He ions on AUG and heating of the background plasma with ICRF, the magnetic field was reduced to 2.8T in pulse #34704, which resulted in shifting the ^{3}He cyclotron resonance off-axis to the HFS at $\rho_{pol} \approx 0.3$ and reducing ^{3}He fast-ion energies. ^{3}He puffs with a puff rate of 2.3x10^{20} el/s were applied every 0.5s, resulting in a ^{3}He concentration of ~0.5-1%. The ICRF power was increased in steps: 0.9MW, 1.9MW and 2.5MW, see Fig. 2(b). Consequently, the plasma stored energy increased from ~0.3MJ during the NBI-only phase (P_{NBI} = 8MW) to ~0.4MJ during the ICRF+NBI phase.

We also note a gradual increase of T_e measured at $\rho_{pol} \approx 0.2$, which is consistent with the dominant collisional electron heating from energetic ^{3}He ions at such low ^{3}He concentrations. Furthermore, lower W levels were observed in this off-axis discharge when compared to on-axis discharges from this series of shots. CXRS measurements of energetic ^{3}He ions in this discharge were analyzed in [45] and the measured spectra were shown to agree well with the modelled spectra using the ^{3}He distribution functions predicted by the TORIC-SSFPQL modelling, yielding the ^{3}He effective temperatures $T_\perp \approx$ 500 keV and $T_\parallel \approx$ 15 keV at $\rho_{pol} \approx 0.3$.

An interesting observation is the appearance of ~90-100 kHz MHD modes in the last phase of the discharge with ICRF heating only. The so developed HFS off-axis ^{3}He heating with the three-ion species scenario on AUG

is highly relevant for H-mode studies in non-active ITER plasmas, for which an option is an equivalent ^{3}He minority heating in H-^{4}He mixed plasmas as has been recently suggested [46].

5. IMPROVED DIAGNOSTIC CONVERAGE

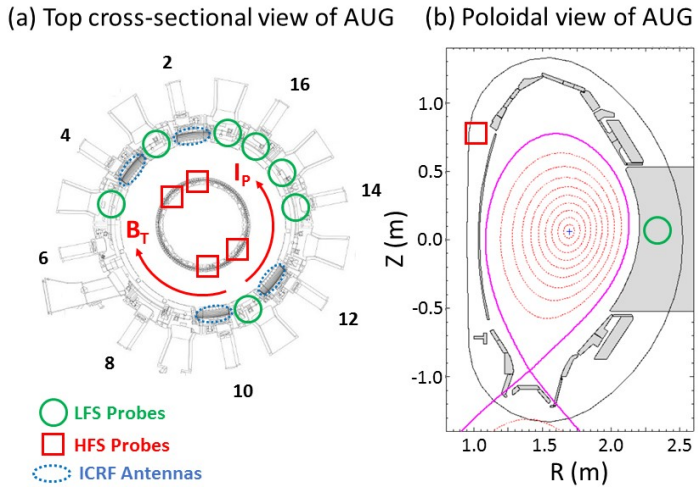

FIG. 3: (a) top and (b) poloidal cross-sectional views of the AUG. The positions of the low-field side (LFS) and the high-field side (HFS) B-dot probes is shown. The HFS probes are positioned radially opposite to the ICRF antennas.

The progress achieved in understanding the interactions between ICRF waves and magnetized plasmas has been substantially supported by new diagnostics.

These include the already mentioned density measurement by x-mode reflectometry embedded in the antenna [40], RF probes to characterize the radiation spectrum of the ICRF-antennas during plasma discharges and the ICE [47], shunts for measurements of RF- and DC-currents to the antenna limiters [9], additional spectroscopic lines of sight measuring WI-line emission and RF current probes in the 3-strap ICRF antennas to provide information on the phasing between central and outer straps [9].

The RF probes consist of inductors that directly detect the magnetic field component of the ICRF wave field and provide information on the wave amplitude, wavenumber, and polarization. The probe coverage inside the ASDEX Upgrade torus is extensive (Fig. 3) and includes locations on the high- and the low-field side. A field-aligned probe array is installed to measure the parallel wavenumber of the ICRF wave [47]. An additional probe pair is available for radial scans on the low-field side manipulator [48]. The probes' outputs are sampled by logarithmic RF detectors [9] that measure both the amplitude and the phase difference between a pair of probes. A fast data acquisition system is used to measure wave frequency spectra for ion cyclotron emission studies [49].

6. DEVELOPMENTS ON IShTAR

IShTAR is a device to investigate antenna-plasma interactions [10]. It consists of a main vacuum vessel (1m diameter, 1m lengh) encircled by two big magnetic field coils in a Helmholz type configuration and containing an ICRF antenna. This vessel is connected to a helicon plasma source (0.4 diameter, 1m length) with 5 smaller magnetic field coils.

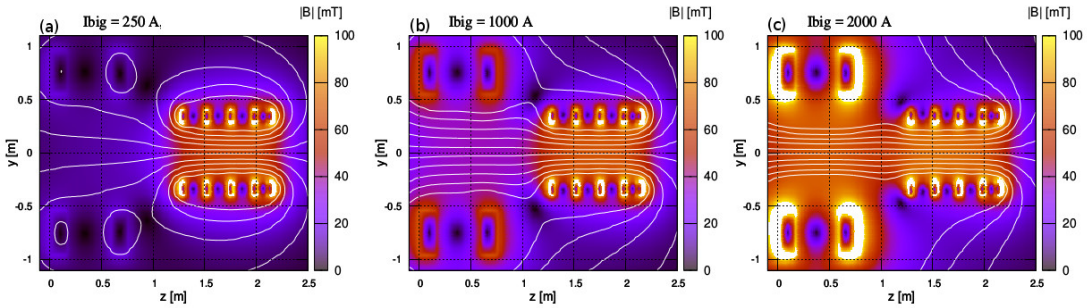

Fig. 4.(a) - (c) Change of magnetic field topology and strength in the main vessel of IShTAR experiment as a function of the current in the big set of coils (Ibig). The current in the small set of coils is kept constant at 1000 A.

The machine performance was improved to achieve the high density and radially uniform plasma in front of the ICRF antenna needed for the sheath studies. The magnetic field topology and its strength determines the plasma flow from the helicon source towards the ICRF antenna. Optimisation consisted in varying the currents in the big and small set of coils. From magnetic mapping one would expect that compression of magnetic field lines in the main vacuum vessel, as it shown in Fig. 4 (a) - (c), should lead to a higher plasma density in that part of the machine than in the helicon plasma source. The results however, show a systematic reduction in density when the magnetic topology changes from Fig. 4(a) to (c), as shown in Fig. 5. This suggests that a magnetic field topology

with field lines diverging outward from the plasma source, is more favourable for the plasma flow than simple straight magnetic field lines with zero divergence. Such an effect also finds implication in magnetic nozzles of plasma propulsion systems.

To benchmark the theoretical tools for the studies of the ICRF antenna-plasma interaction a diagnostic is being developed to directly measure the electric fields in the sheath near the antenna structures. The development of a dedicated diagnostic technique for such a specific problem requires easy access and sufficient operational time, which IShTAR provides. The geometry is simplified but nevertheless mimics the physics phenomena of interest. The diagnostic is based on the Stark effect which modifies the emission spectra of the atoms when exposed to external electric fields. The effect is more evident for hydrogen and helium atoms. The relative shift of the spectral line from its unperturbed wavelength, allows us to extract the amplitude and direction of the electric field that excited helium atoms are submitted to.

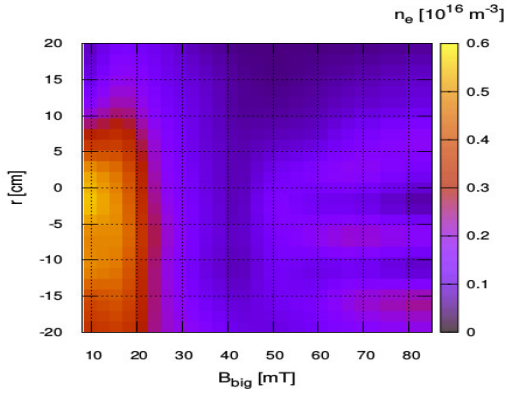

FIG. 5. Radial profile of the plasma density in the main vacuum vessel as a function of the magnetic field in the center of the main vessel. The range of magnetic fields Bbig corresponds to the change of current in the set of big coils Ibig in Fig.4. (a)-(c).

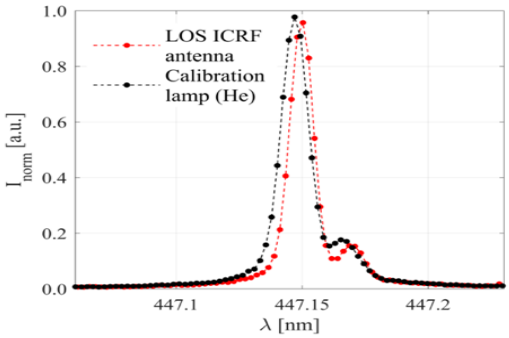

FIG. 6. Time averaged spectra over 10.5 s in 19 discharges at the ICRF antenna view-location, normalized for comparison with the spectra from helium calibration lamp demonstrate the shift from the unperturbed spectral line position corresponding to electric field strength of E = 3.4 ± 0.3 kV cm^{-1} [50]

One way of applying Stark spectroscopy is on the passive optical emission spectra recorded with a single fibre coupled to a high-resolution spectrometer (the spectral resolution is 0.0023 nm per pixel). With this technique we have collected the emitted light from the sheath around the leading edge of IShTAR's ICRF antenna box. Since the ICRF antenna was employed in the discharge scenario, the unperturbed spectra were recorded from a helium calibration lamp [Fig. 6]. With the maximum power delivered to the ICRF antenna, which was of the order of 1 kW, the relative shift of the spectral line profile detected was corresponding to electric field of E = 3.4 ± 0.3 kV cm^{-1} [50] Even though the described effect is localized to the regions where the electric fields are present and sufficiently strong, the measurements are time-averaged and volume integrated. To improve the method, a newly designed optical head with a fibre-bundle instead of a single fibre in combination of a local helium gas-puff will provide spatially resolved electric field distribution in the sheath.

As a next step, we are implementing a laser-aided spectroscopy, as it is superior to the passive optical emission, in terms of spectral, spatial and temporal resolution of the recorded spectra. Doppler-free saturation spectroscopy is such a technique currently in the implementation phase in IShTAR. Spectra recorded in this way will allow us to obtain electric field measurements with higher accuracy and better sensitivity. [51, 52, 53].

Another approach to obtain RF sheath electric field of the ICRF antenna is a combined experimental-numerical method. In the experimental part, the ICRF magnetic field components were measured in front of the antenna with an array of B-dot probes driven on a manipulator. The resulting experimental profiles are compared to calculations performed in COMSOL software [54], from which the E fields can then also be derived.

IShTAR's ICRF antenna is modelled with high geometrical precision (± 0.1 mm). Good qualitative agreement of numerical and experimental results allows us to consider the model reliable and to trust electric field values retrieved from the simulation. A vacuum approximation of the parallel electric field distribution is obtained from the COMSOL model and used as an input to test a code that calculates DC voltages in the sheath. Work on plasma implementation into the IShTAR model is being carried out. The presence of a Lower Hybrid (LH) resonance complicates numerical calculations. A common method of avoiding this resonance by replacing part of the low density plasma with a vacuum layer is however not adequate for IShTAR, since the whole plasma volume in the device is low density SOL-like plasma. Further analysis thus is needed to achieve reliable numerical results.

Local density measurements at the very edge of the plasma near the antenna limiters and even in the limiters shadow (~ $1x10^{15}$ m^{-3}) have been performed with RF compensated planar Langmuir probes. The probes dimensions had to be big enough (1 mm thick, 5 mm radius) to obtain tolerable signal-to-noise ratio and at the same time small enough not to perturb plasma too much when measuring very close (~ 2 cm) to metallic antenna structures.

7. SUMMARY

Significant progress has been achieved in applying ICRF power to experiments with metallic walls as shown on ASDEX Upgrade, by optimizing the antenna geometry. This progress was associated with advances in understanding and modelling. It was strongly supported by additional diagnostics and an accompanying programme on IShTAR.

ACKNOWLEDGEMENTS

This work has been carried out within the framework of the EUROfusion Consortium and has received funding from the Euratom research and training programme 2014-2018 under grant agreement No 633053. The views and opinions expressed herein do not necessarily reflect those of the European Commission.

REFERENCES

[1] J.-M. Noterdaeme et al., AIP Conf. Proc. (1993) 289, 12
[2] J.-M. Noterdaeme et al., 16th IAEA Conf. on Fusion Energy, (1996), IAEA, Vol. 3, 335
[3] J.-M. Noterdaeme et al., Contr. Fus. and Plasma Phys., (1999), EPS, Vol. 23J, 1561
[4] J.-M. Noterdaeme et al., AIP Conf. Proc. (1995) 355, 47
[5] Th. Pütterich et al., "The ITER baseline scenario investigated at ASDEX Upgrade", this conf., EX/P8-4
[6] M. Garcia-Munoz et al., Nuclear Fusion 51, 10 (2011), 103013
[7] D. Douai et al., Journ. of Nucl. Mat. 463 (2015) 150
[8] J.-M. Noterdaeme et al., Fus. Eng. Des. 24 (1994), 65
[9] Faugel, H. et al., "An overview of the in-vessel ICRF-diagnostics in the ASDEX Upgrade tokamak", SOFT 2018, to be published in Fus. Eng. Des.
[10] K. Crombé et al., AIP Conf. Proc. (2015) 1689, 030006
[11] Ye.O. Kazakov et al., Nucl. Fusion 55 (2015) 032001
[12] Ye.O. Kazakov et al., Phys. Plasmas 22 (2015) 082511
[13] Ye.O. Kazakov et al., Nature Physics 13 (2017) 973
[14] V. Bobkov et al., J. Nucl. Mater. 363–365 (2007) 122
[15] R. Dux et al., J. Nucl. Mater. 363–365 (2007) 112–116
[16] V. Bobkov et al., Nucl. Fusion 50 (2010) 035004
[17] L. Colas et al., EPJ Web of Conf. 157 (2017) 01001
[18] V. Bobkov et al., Nucl. Fusion 53 (2013) 093018
[19] H. Fünfgelder et al., Fus. Eng. Des. 123 (2017) 40
[20] V. Bobkov et al., "Impact of ICRF on the scrape-off layer and on plasma wall interactions: from present experiments to fusion reactor" subm. to Nucl. Mat. and Energy (2018)
[21] V. Bobkov et al., Plasma Phys. Contr. Fus. 59 (2017) 014022
[22] V. Bobkov et al., EPJ Web of Conf. 157 (2017) 03005
[23] W. Tierens et al., Nucl. Fusion 57 (2017) 116034
[24] W. Tierens et al., submitted to Nucl. Fusion
[25] J. Jacquot et al., AIP Conference Proceedings 2015
[26] L. Colas et al., "Perfectly Matched Layers for time-harmonic electromagnetic wave propagation in curved gyrotropic media" submitted to Journal of Computational Physics
[27] I. Stepanov et al., Nucl. Fusion 55 (2015) 113003
[28] V. Bobkov et al AIP Conf. Proc. (2015) 1689 030004
[29] Y. Feng et al., Contrib. to Plasma Phys. 44 (2004) 57
[30] M. Brambilla et al., Plasma Phys. Contr. Fus. 31 (1989) 723
[31] W. Zhang et al., Plasma Phys. Contr. Fus. 59 (2017) 075004
[32] W. Zhang et al., Nuclear Fusion 56 (2016) 036007
[33] W. Zhang et al., EPJ Web of Conf. (2017) 157 03066
[34] W. Zhang et al., Nuclear Fusion 57 (2017) 056042
[35] W. Zhang et al., "Scrape-off layer density tailoring with local gas puffing to maximize ICRF power coupling in ITER" submitted to Nucl. Mat. and Energy (2018)
[36] W. Zhang et al., "EMC3-EIRENE modelling of edge plasma to improve the ICRF coupling with local gas puffing in DEMO" Nucl. Fus. (2018) accepted. for publication
[37] W. Zhang et al., Plasma Phys. Contr. Fus. 58 (2016) 095005
[38] J. Jacquot et al., Physics of Plasmas 21 (2014) 061509
[39] W. Zhang et al., 2017 Nuclear Fusion 57 (2017) 116048
[40] D.E. Aguiam et al., Rev. Sci. Instrum. 87 (2016) 11E722
[41] W. Zhang et al., "Blob distortion by radio-frequency convective cells" (2018) to be subm. to Phys. Rev. Letters
[42] B. D. Dudson et al., Computer Physics Communications 180 (2009) 1467-80
[43] Ye.O. Kazakov et al., 45th EPS Conf. Plasma Phys. (2018) ECA 42A, P5.1047
[44] M. Mantsinen et al., AIP Conf. Proc. (2015) 1689, 030005
[45] A. Kappatou et al., 45th EPS Conf. Plasma Phys. (2018) ECA 42A, O2.102
[46] M. Schneider et al., EPJ Web. Conf. 157 (2017) 03046
[47] R. Ochoukov et al., Rev. Sci. Instrum. 86 (2015) 115112
[48] R. Ochoukov et al., EPJ Web Conf. 157 (2017) 03038
[49] R. Ochoukov et al., Rev. Sci. Instrum. 89 (2018) 10J101
[50] A. Kostic et al., Rev. Sci. Instrum. 89 (2018) 10D115
[51] K. Crombé et al., 44th EPS Conf. Plasma Phys. (2017) ECA Vol. 41F, P5.144
[52] K. Crombé et al., 45th EPS EPS Conf. Plasma Phys. (2017) ECA Vol. 42A, P4.1010
[53] E. H. Martin et al., Rev. Sci. Instrum. 87 (2016) 11E402
[54] M. Usoltceva et al., EPJ Web of Conf. 157 (2017) 03058